# Supplementary Materials for

## Switching the Oxygen Evolution Mechanism on Atomically Dispersed Ru for Enhanced Acidic Reaction Kinetics

Yixin Hao[a], Sung-Fu Hung[b], Wen-Jing Zeng[b], Ye Wang[a], Chenchen Zhang[c], Chun-Han Kuo[d], Luqi Wang[a], Sheng Zhao[a], Ying Zhang[c], Han-Yi Chen[d] and Shengjie Peng[a]*

[a]College of Materials Science and Technology, Nanjing University of Aeronautics and Astronautics, Nanjing 210016, China.
[b]Department of Applied Chemistry, National Yang Ming Chiao Tung University, Hsinchu 300, Taiwan.
[c]Key Laboratory of Synthetic and Biological Colloids, Ministry of Education, School of Chemical and Material Engineering, Jiangnan University, Wuxi, Jiangsu 214122, China.
[d]Department of Materials Science and Engineering, National Tsing Hua University, Hsinchu 30013, Taiwan.
*Email: pengshengjie@nuaa.edu.cn

**This PDF file includes:**

## Experimental section

Materials. Cobalt acetate tetrahydrate ($C_4H_6CoO_4 \cdot 4H_2O$), Glycerol ($C_3H_8O_3$), and Ruthenium chloride anhydrous ($RuCl_3$) were purchased from Macklin. Methanol (GR) was purchased from Sigma-Aldrich (Shanghai, China). Nafion solution was obtained from DuPont company. Milli-Q ultrapure water was used in all experiments. All of the above chemicals were analytical grade and used as received without further purification.

Preparation of glycerolatocobalt (CoGly). 1.0 g cobalt acetate tetra-hydrate was added into a 50 mL Teflon-lined autoclave containing 30 mL glycerol under 5 h magnetic stirring to give a uniform slurry. Then the reactor was heated to 180 ℃ and maintained for 4 h. After that, the obtained viscous mixture was washed with ethanol repeatedly and dried at 60 ℃.

Preparation of $Co_3O_4$ with different metal defect concentrations. The obtained pink powder was calcined in air at 300 ℃ for 4 h and the product was denoted as $Co_3O_4$-$V_{Co}$. The comparison samples prepared at 500 ℃ and 700 ℃ were labeled as $Co_3O_4$-500 and $Co_3O_4$-700, respectively.

Preparation of $Ru_{(anc)}$-$Co_3O_4$ (atomic ruthenium-anchored cobalt oxides) with different ruthenium atom concentrations. 50 mg of cobalt glycerol was stirred with 1, 3, 5 and 7 mM of $RuCl_3$ alcohol solution for 14 h at room temperature, washed by centrifugation, dried under vacuum and calcined at 300 ℃ for 4 h in air to obtain $Ru_{(anc)}$-$Co_3O_4$. the resultant products were denoted as $Ru_{(anc)}$-$Co_3O_4$-1, $Ru_{(anc)}$-$Co_3O_4$-3, $Ru_{(anc)}$-$Co_3O_4$-5, and $Ru_{(anc)}$-$Co_3O_4$-7, respectively. Mass loading a of the Ru element was determined by ICP and the relevant data are shown in table S1.

Preparation of $Ru_{(ads)}$-$Co_3O_4$ (atomic ruthenium-adsorbed cobalt oxides). To prevent cobalt vacancies from trapping ruthenium single atoms, well-crystallized $Co_3O_4$-700 was used as the parent precusor for adsorption of ruthenium single atoms, as detailed in the following experiments. 50 mg of $Co_3O_4$-700 was stirred with 5 mM of $RuCl_3$ alcohol solution for 14 h at room temperature, washed by centrifugation, dried under vacuum and calcined at 200 ℃ for 1 h in air to obtain $Ru_{(ads)}$-$Co_3O_4$.

## Material Characterizations

General characterizations. The morphologies of catalysts were observed by SEM (SEM, JEOL JSM-6700 F), HR-TEM (TEM-EDX, Philips Tecnai F20, 200 kV), and aberration-corrected transmission electron microscope (ACTEM, JEOL JEM-ARM200F). The elemental compositions were analyzed by ICP (ICP-OES, inductively coupled plasma optical emission spectroscopy). The crystal structure of the samples was characterized by X-ray powder diffraction (XRD, Bruker D8 Discover) with Cu Kα radiation (λ = 1.5418 Å). The chemical valence state and surface atomic ratio were collected by X-ray photoelectron spectroscopy (XPS, ESCALAB 250Xi). The extended X-ray absorption fine structure (EXAFS) was measured at Taiwan Photon Source (TPS) beamline, 44A Quick-scanning X-ray absorption spectroscopy (XAS), in National Synchrotron Radiation Research Center (NSRRC), Hsinchu, Taiwan. The Electron paramagnetic resonance (EPR, Bruker EMX-6/1) was used to obtain the information about cationic vacancies concentration. Resonance Raman spectra were conducted on a confocal Raman microscope (Invia Reflex) with 532 nm wavelength at the sample surface.

Electrochemical in situ ATR-SEIRAS experiments. ATR-SEIRAS measurements were performed by a Nicolet iS50 FT-IR spectrometer with a liquid nitrogen cooled MCT detector and a fixed angle IR optical path. The spectral resolution of the measurements was 8 $cm^{-1}$ and 32 interferograms were added for each spectrum. The working electrode was prepared in two main steps, firstly by chemically depositing an ultra-thin Au film on a silicon crystal for enhancing the IR signal and conducting electrons; then a catalyst slurry was dropped onto the Au surface with a loading of 0.1 mg $cm^{-2}$ (catalyst slurry ratio: 7 mg catalyst, 3 mg carbon black dispersed in 1 mL ethanol and 50 μL Nafion added (sonication for 30 min). The prepared working electrodes were mounted in an electrochemical three-electrode cell with Ag/AgCl as the reference electrode, Pt foil as the counter electrode, and the Ar-saturated 0.5 M $H_2SO_4$ was used as the electrolyte for the OER reaction. All measurements were carried out using linear scanning voltammetry (LSV) to analyse the OER reaction intermediates at different potentials, respectively.

In situ XAFS measurements. In-situ X-ray absorption spectroscopy including XANES and EXAFS at Ru K-edge were collected in total-fluorescence-yield mode using a silicon drift detector in BL-44A at National Synchrotron Radiation Research Center (NSRRC), Taiwan. The measurement in a typical three-electrode setup as the same condition in electrochemical characterization case was performed in a specially designed Teflon container with a window sealed by Kepton tape. The scan range was kept in an energy range of 21900-22800 eV for Ru

K-edge. Subtracting the baseline of pre-edge and normalizing that of post-edge obtained the spectra. EXAFS analysis was conducted using Fourier transform on k2-weighted EXAFS oscillations. All EXAFS spectra are presented without phase correction.

**Electrochemical Measurement**

The electrochemical characterizations were conducted in a three-electrode system with Pt plate and saturated $Hg/HgSO_4$ electrode used as the counter electrode and reference electrode, respectively. The measurements were carried out on an Autolab electrochemical workstation (Autolab Instrument) at room temperature. The active catalyst, conductive agent (carbon black) and binder (Polyvinylidene fluoride, PVDF) were mixed in a weight ratio of 7:2:1, and N-methyl-2-pyrrolidone (NMP) was used as the solvent. The viscous slurry was uniformly coated on carbon paper and dried under infrared light. The measured potentials versus $Hg/Hg_2SO_4$ were converted to the reversible hydrogen electrode (vs. RHE) according to the following equation: $E_{RHE} = E_{Hg/Hg2SO4} + 0.616\ V + 0.0591\ pH$. The potentials were corrected through a manual post-correction approach according to the formula: $E=E_{applied} - iR$, where $i$ is the current flowing through the cell, and $R$ is the ohmic resistance of the cell. Electrochemical impedance spectroscopy (EIS) measurements were carried out in the frequency range of 0.01-100 kHz with AC amplitude of 5 mV. The double-layer capacitance ($C_{dl}$) was obtained by collecting CV curves with scan rates of 20 to 100 mV $s^{-1}$.

Calculation of the specific current density per electrochemically active surface area (ECSA). The electrochemical double-layer capacitance ($C_{dl}$) was determined by measuring the capacitive current associated with double-layer charging from the scan-rate dependence of cyclic voltammetry stripping. The $C_{dl}$ was estimated by plotting the $\Delta j = (j_a - j_c)$, where $j_c$ and $j_a$ are the cathodic and anodic current densities, respectively, against the scan rate, in which the slope was twice that of $C_{dl}$.

The turnover frequency (TOF) of the catalysts was calculated using following equation:

$$TOF(formate\ h^{-1}) = 3600 \times TOF(formate\ S^{-1})$$
$$= 3600 \times \frac{formate\ turnovers\ per\ A_{geo}}{Active\ sites\ per\ A_{geo}}$$

The formate turnover per geometric area was obtained from the geometric current density for the LSV polarization curves according to equation:

$$Formate\ turnover\ per\ A_{geo} = j_{geo} \times \frac{1\ C\ s^{-1}}{1000\ mA} \times \frac{1\ mol}{96485.3\ C} \times \frac{1}{4} \times \frac{6.023 \times 10^{23}}{1\ mol\ O_2}$$

All Ru atoms were assumed to be active sites. Therefore, the number of active sites per geometric area equals the number of Ru atoms per geometric area, which can be calculated from the results of the ICP-OES analysis.

The mass activity ($j_{mass\ activity}$) of the catalysts was determined using equation (1):

$$j_{\text{mass activity}} = \frac{j_{geo} \times A_{geo}}{m_{Ru}}$$

where $m_{Ru}$ is the calculated Ru mass loaded onto carbon paper based on the results of ICP-OES analysis, $A_{geo}$ is the geometric area and $j_{geo}$ is the geometric current density.

The specific current density per ECSA ($j_s$) was calculated as shown in equation (2):

$$j_s = \frac{j_{geo}}{ECSA}$$

where $j_{geo}$ is the geometric current density.

In situ EIS measurements. In situ characterization tandem electrochemical operation was carried out at the specified potential to obtain the surface chemical composition and structural information of the materials. EIS tests were performed at different potentials in the frequency range of 0.01-100,000 Hz.

Pulse voltammetry (PV) were performed while following current over time (1,600 rpm RDE). The potential was kept at a low potential ($E_l$ = 1.15 V vs. Ag/AgCl), then switched and kept at a higher potential ($E_h$) before returning to El. This cycle was repeated while increasing $E_h$ from 1.22 V to 1.30 V in 20 mV/step and keep $E_l$ unchanged. Charge related to the potential step was calculated by integrating the current pulse over time accounting for the background current signal.

pH-dependence measurement. The electrolyte was prepared by adding the components of Britton-Robinson buffer (0.4 M each of phosphate, borate, and acetate) to a 0.5 M $Na_2SO_4$ solution, and the pH was then adjusted to the desired value by addition of $H_2SO_4$. All glassware was sonicated in ultrapure water directly before performing electrochemical.

**Calculation methods**

All DFT calculations were performed using the Vienna Ab initio Simulation Package (VASP)[1]. The projector augmented wave (PAW)[2] pseudopotential with the PBE[3] generalized gradient approximation (GGA) exchange correlation function was utilized in the computations. All energetics of metal oxides were calculated using the DFT with the Hubbard-U framework (DFT+U) to account for strongly localized d-electrons for Co. The Hubbard-U correction terms were at $U_{eff}$(Co) = 3.32 eV as obtained via linear response theory. The cutoff energy of the plane waves basis set was 500 eV and a Monkhorst-Pack mesh of 3×3×1 was used in K-sampling. All structures were spin polarized and all atoms were fully relaxed with the energy convergence tolerance of $10^{-5}$ eV per atom, and the final force on each atom was < 0.05 eV $Å^{-1}$.

The adsorption energy of reaction intermediates, can be computed using the following Equation (1):

$$\Delta G_{ads} = E_{ads} - E_{*} + \Delta E_{ZPE} - T\Delta S$$

Where ads = (OH*, O*, OOH*), and ($E_{ads} - E_{*}$) is the binding energy, $\Delta E_{ZPE}$ is the zero-point energy change, $\Delta S$ is the entropy change. In this work, the values of $\Delta E_{ZPE}$ and $\Delta S$ were obtained by vibration frequency calculation.

The Gibbs free energy of the five reaction steps can be calculated by the following four Equations (2)-(5):

$$H_2O + {}^{*} \leftrightarrow HO^{*} + H^{+} + e^{-}$$

$$\Delta G_1 = \Delta G_{HO^{*}} + G_H - \Delta G_{*} - G_{H_2O} - eU$$

$$HO^{*} \leftrightarrow O^{*} + H^{+} + e^{-}$$

$$\Delta G_2 = \Delta G_{O^{*}} - \Delta G_{HO^{*}} + G_H - eU$$

$$O^{*} + H_2O \leftrightarrow OOH^{*} + H^{+} + e^{-}$$

$$\Delta G_3 = \Delta G_{OOH^{*}} + G_H - \Delta G_{O^{*}} - G_{H_2O} - eU$$

$$OOH^{*} \leftrightarrow {}^{*} + O_2 + H^{+} + e^{-}$$

$$\Delta G_4 = \Delta G_{*} - \Delta G_{OOH^{*}} + G_H + G_{O_2} - eU$$

In this work, $\Delta G_{1-4}$ were calculated at U=0.


1. Kresse G. & Furthmüller J. Efficient iterative schemes for ab initio total-energy calculations using a plane-wave basis set. *Phy. Rev. B* **54**, 11169-11186 (1996).
2. Blöchl P. E. Projector augmented-wave method. *Phy. Rev. B* **50**, 17953-17979 (1994).
3. Perdew J. P., Burke K. & Ernzerhof M. Generalized gradient approximation made simple. *Phy. Rev. Lett.* **77**, 3865-3868 (1996).

## Figures and tables

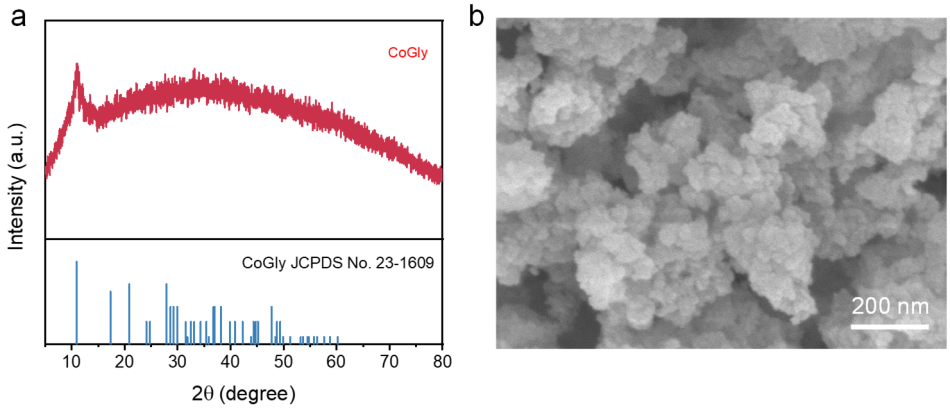


**Figure S1.** (a) X-ray diffraction pattern and (b) SEM image of glycerolatocobalt (CoGly).

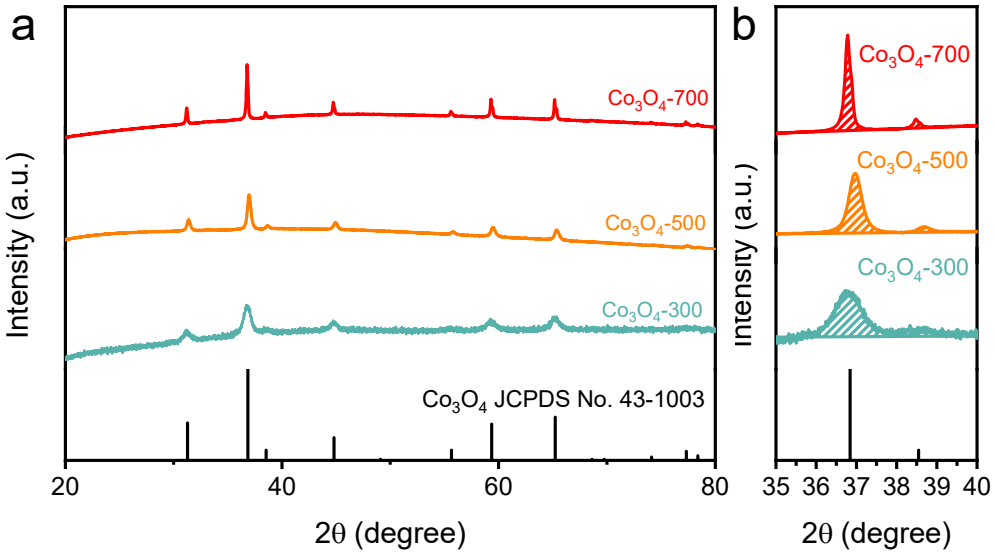


**Figure S2.** (a-b) XRD patterns of $Co_3O_4$ formed by CoGly at different annealing temperatures.

With increasing the calcination temperature, the diffraction peaks became sharper and stronger, indicating the improved crystallization in nature for the cobalt oxides. The results suggested the formation of cobalt oxide at the temperatures above 300 °C and crystallization was improved at the higher temperature. The results suggested the $Co_3O_4$-$V_{(Co)}$ was formed at 300 °C, and the crystallinity could be improved at higher temperatures.

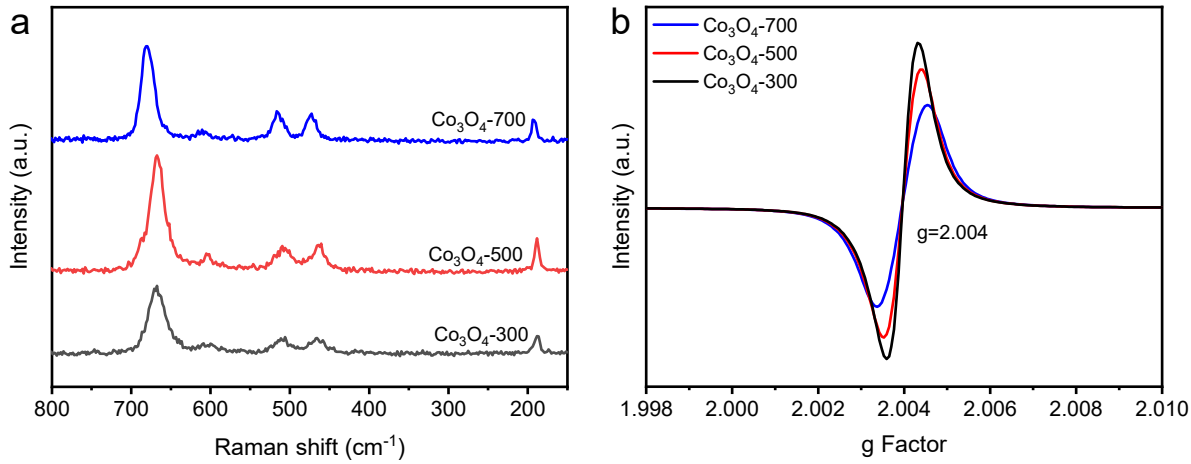


**Figure S3.** (a) Raman spectra and (b) EPR spectra of $Co_3O_4$-300, $Co_3O_4$-500, and $Co_3O_4$-700.

With the increase of calcination temperature, the positive shift of Raman peak indicates that the crystal structure changes from short-range order to long-range order, which is in good agreement with XRD results. It also means that more metal defect sites form at lower temperatures. All samples exhibit electron paramagnetic resonance signal at g = 2.004, which would be associated with the cationic vacancies. $Co_3O_4$-300 exhibits the maximum vacancy concentration, and the vacancy gradually decreased along with the increasing treatment temperature.

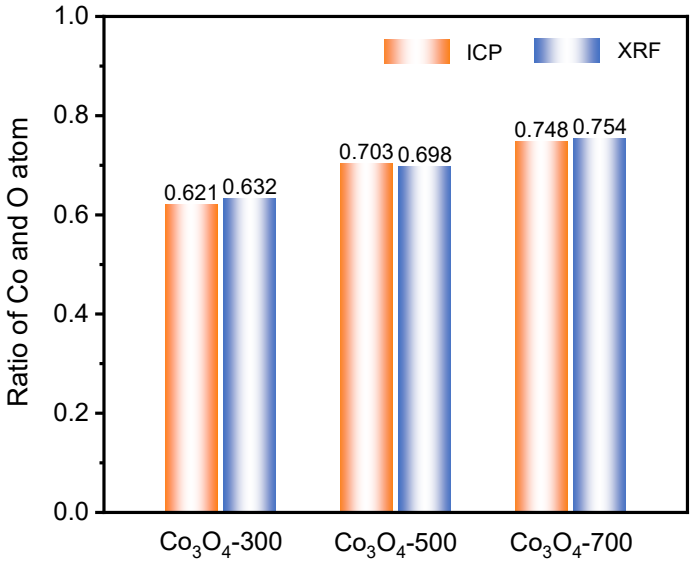


**Figure S4.** the ratios of Co and O atoms of $Co_3O_4$-300, $Co_3O_4$-500, and $Co_3O_4$-700 calculated by X-ray fluorescence spectrometer (XRF) and inductively coupled plasma (ICP) analysis.

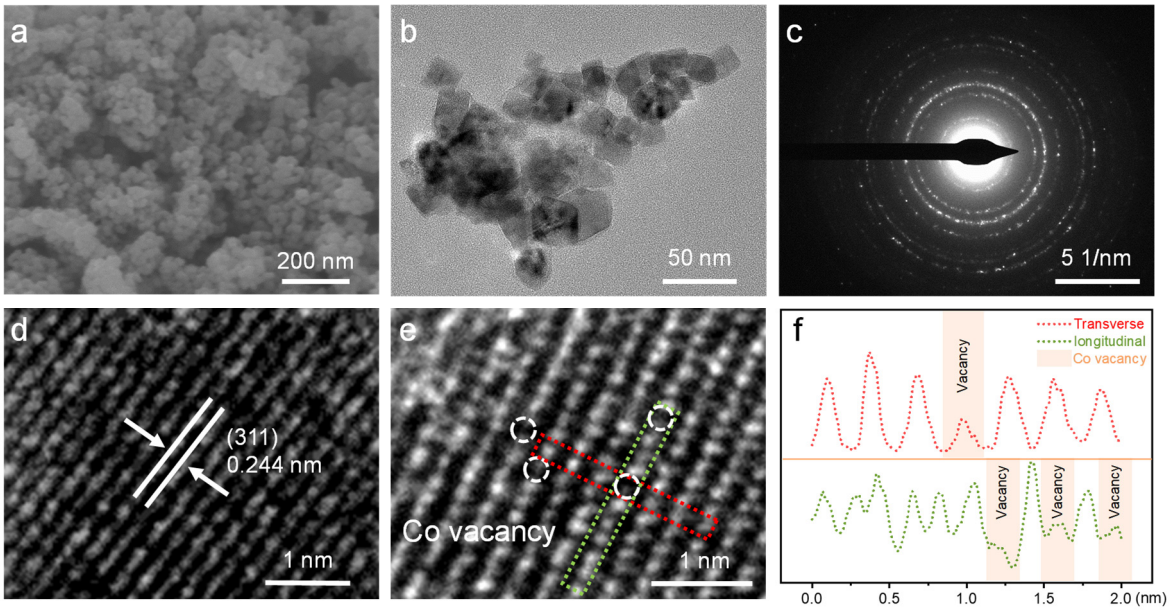


**Figure S5.** (a) SEM image, (b) TEM image (c) corresponding SAED pattern, (d) HRTEM image, (e) atomic-resolution spherical aberration corrected TEM image of $Co_3O_4$-300, (f) intensity profile recorded of corresponding region.

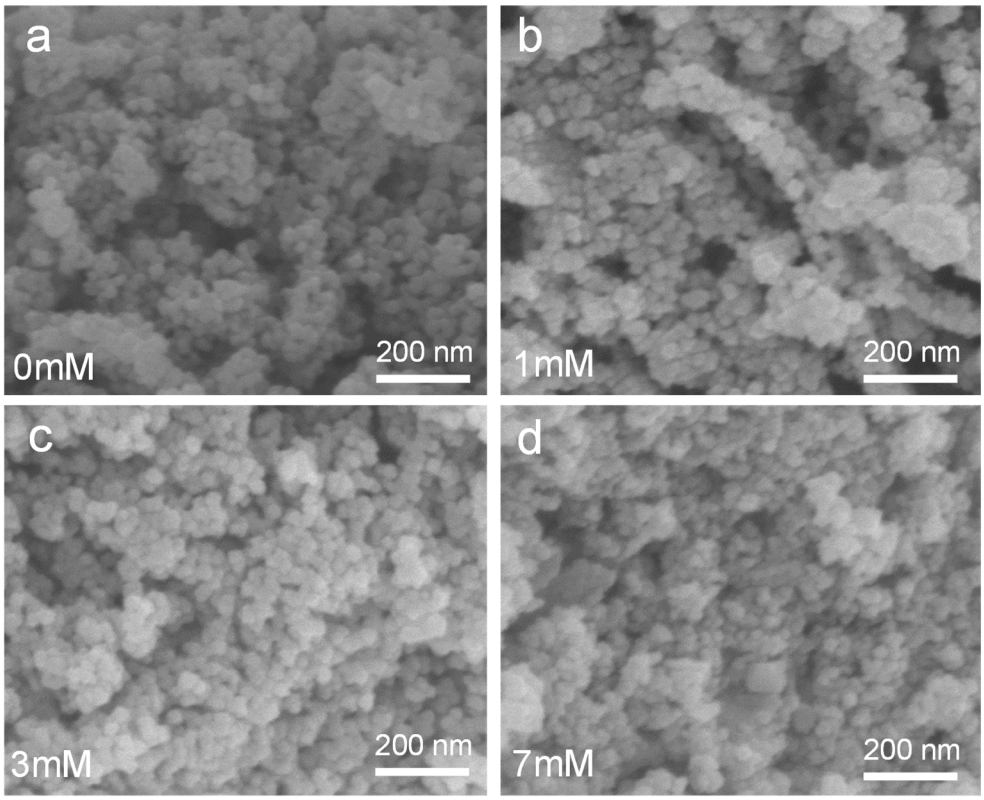


**Figure S6.** SEM images of (a) $Co_3O_4$-$V_{Co}$ nanoparticles, (b) $Ru_{(anc)}$-$Co_3O_4$-1, (c) $Ru_{(anc)}$-$Co_3O_4$-5, and (d) $Ru_{(anc)}$-$Co_3O_4$-7 catalysts.

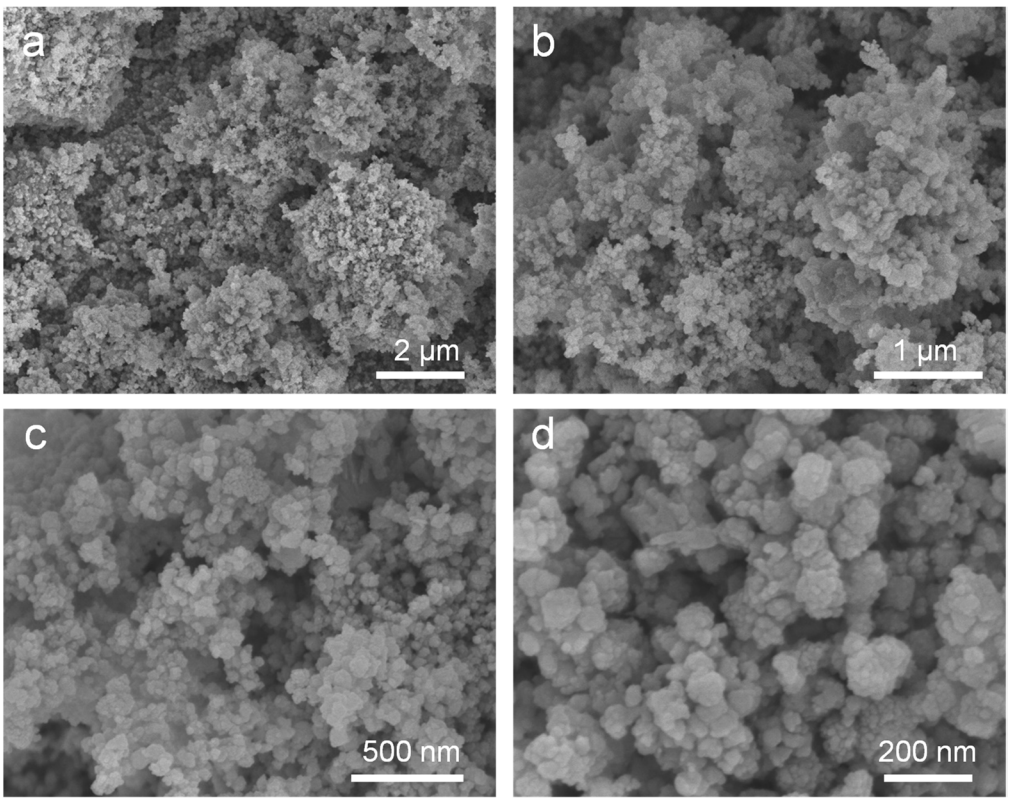


**Figure S7.** (a-d) SEM images of $Ru_{(ads)}$-$Co_3O_4$ catalyst at different magnifications.

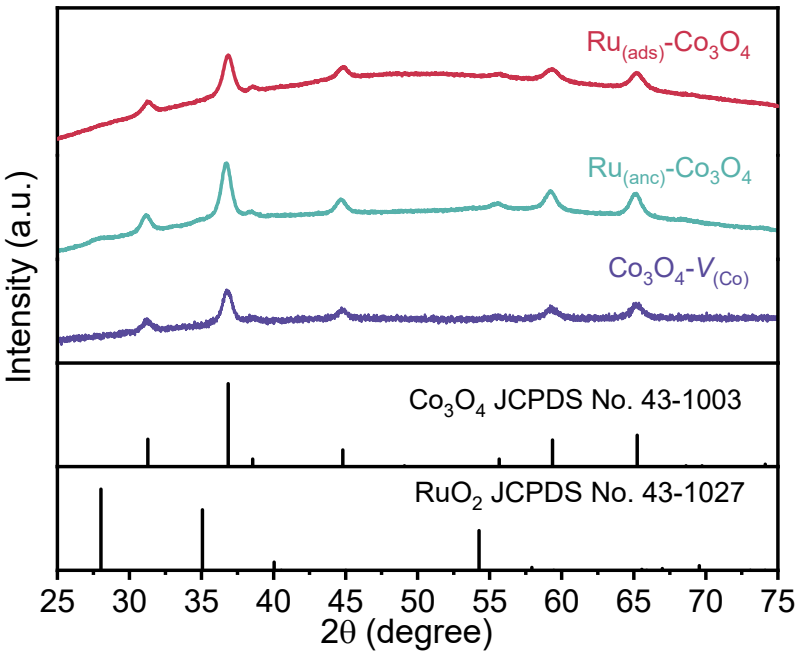


**Figure S8.** XRD patterns of $Ru_{(anc)}$-$Co_3O_4$ and $Ru_{(ads)}$-$Co_3O_4$. No diffraction peaks of ruthenium dioxide were found in either $Ru_{(anc)}$-$Co_3O_4$ or $Ru_{(ads)}$-$Co_3O_4$.

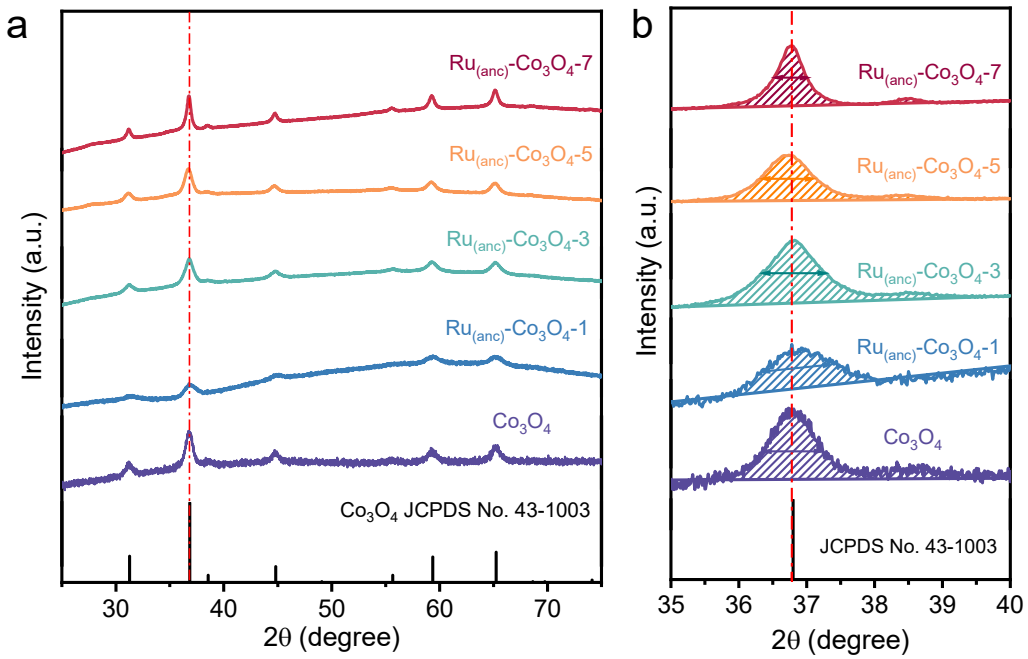


**Figure S9.** (a) XRD patterns of $Co_3O_4$, $Ru_{(anc)}$-$Co_3O_4$-1, $Ru_{(anc)}$-$Co_3O_4$-3, $Ru_{(anc)}$-$Co_3O_4$-5, and $Ru_{(anc)}$-$Co_3O_4$-7, (b) drawing of partial enlargement.

All the diffraction peak of $Ru_{(anc)}$-$Co_3O_4$-X can be assigned to a cubic phase Fd3m(227), indicating the stability of the monatomic parent structure. The enlarged pattern at (311) demonstrates the changes in the cell parameter after Ru incorporation. The crystallinity becomes progressively better as the amount of ruthenium atoms anchored at the vacant sites increases.

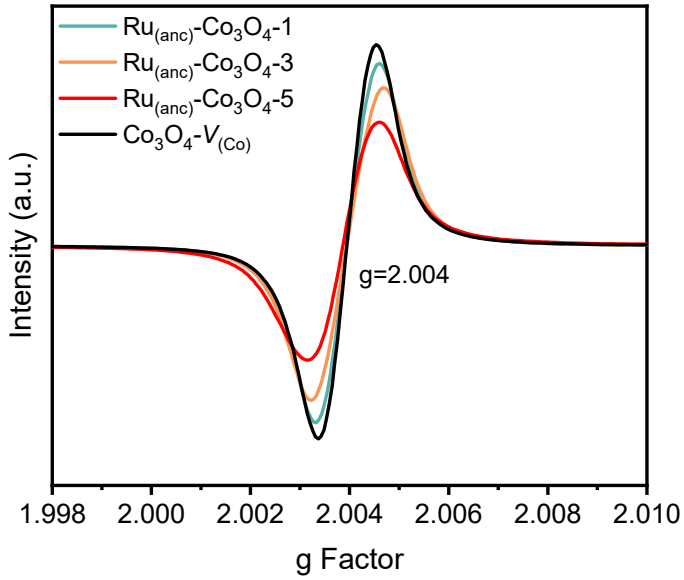


**Figure S10.** The EPR spectra of $Co_3O_4$-$V_{Co}$, $Ru_{(anc)}$-$Co_3O_4$-1, $Ru_{(anc)}$-$Co_3O_4$-3, and $Ru_{(anc)}$-$Co_3O_4$-5 catalysts.

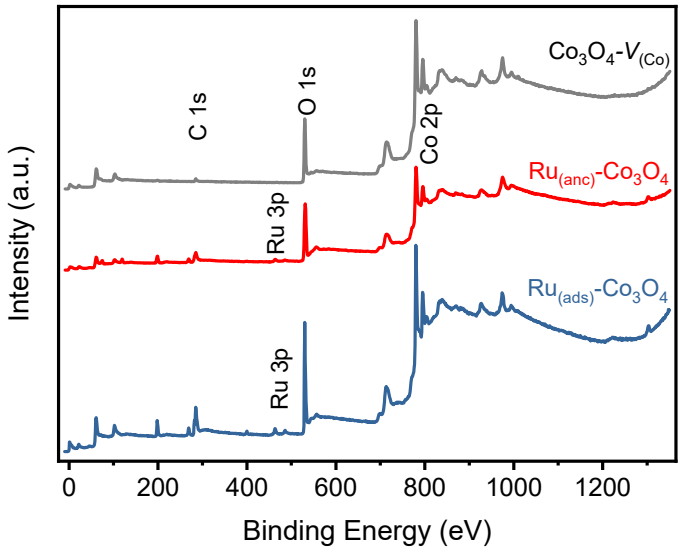


**Figure S11.** Survey XPS spectra of $Co_3O_4$-$V_{Co}$, $Ru_{(ads)}$-$Co_3O_4$ and $Ru_{(anc)}$-$Co_3O_4$.

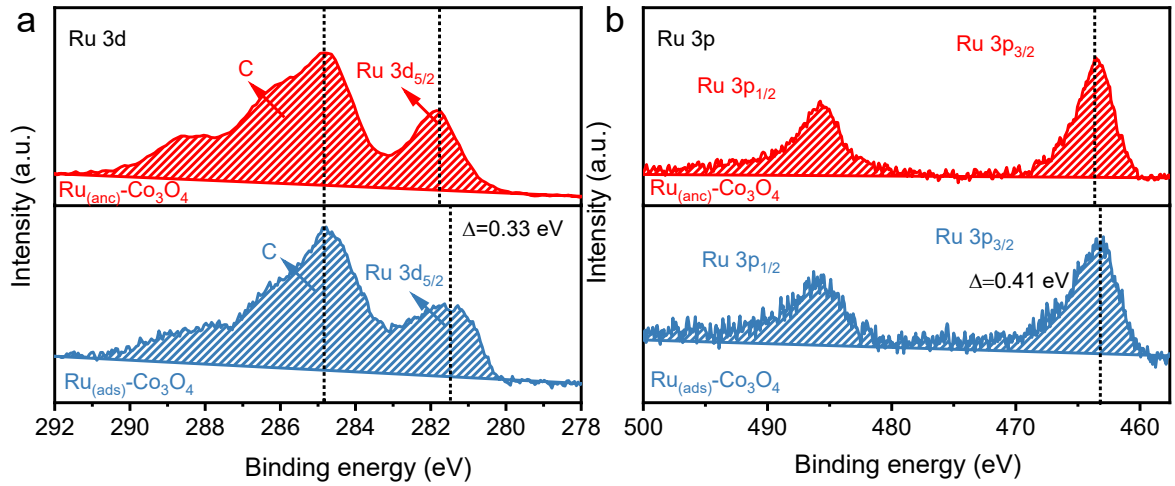


**Figure S12.** (a) Curve-resolved XPS of the Ru 3d region for $Ru_{(ads)}$-$Co_3O_4$ and $Ru_{(anc)}$-$Co_3O_4$. (b) Curve-resolved XPS of the Ru 3p region for $Ru_{(ads)}$-$Co_3O_4$ and $Ru_{(anc)}$-$Co_3O_4$.

The binding energy of Ru 3d5/2, 3d3/2, 3p3/2 and 3p1/2 for $Ru_{(anc)}$-$Co_3O_4$ was positively shifted (~0.33 eV and 0.41 eV) compared with that of $Ru_{(ads)}$-$Co_3O_4$, possibly suggesting that Ru in the catalyst presented a slightly higher oxidation state than that in $Ru_{(ads)}$-$Co_3O_4$ (see the X-ray absorption near-edge spectroscopy (XANES) spectra below for additional evidence).

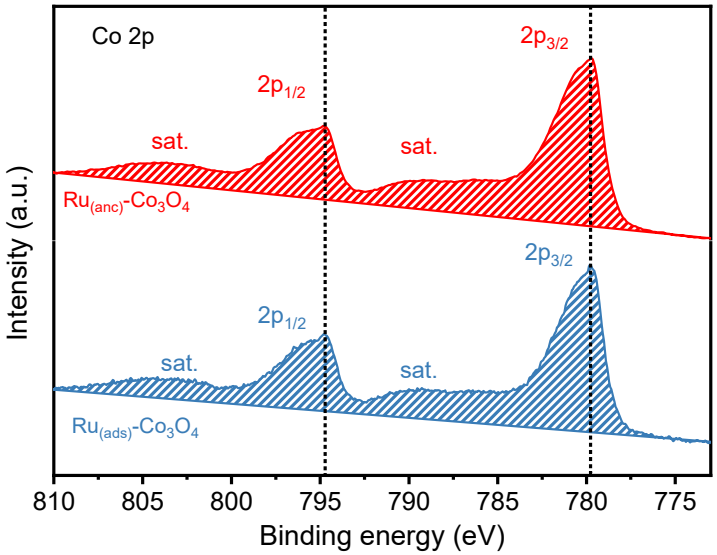


**Figure S13.** XPS spectra of Co 2p for $Ru_{(ads)}$-$Co_3O_4$ and $Ru_{(anc)}$-$Co_3O_4$ catalysts.

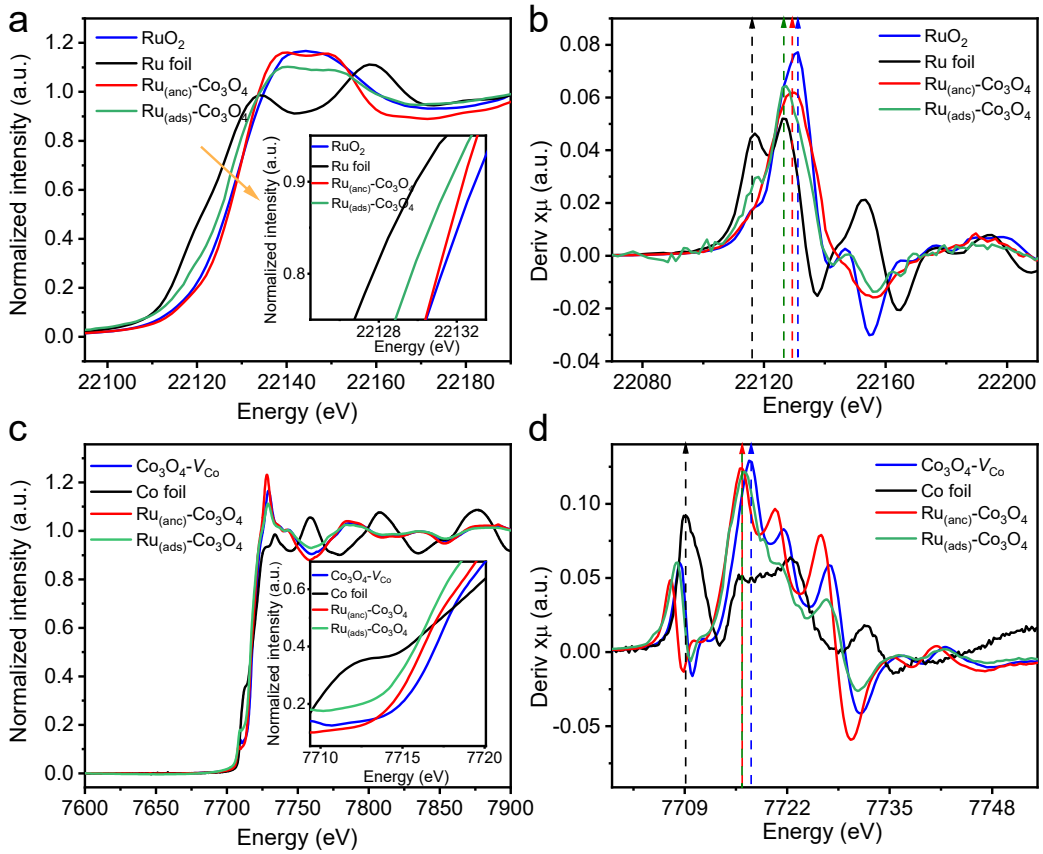


**Figure S14.** (a) The normalized XANES spectra and (b) first derivative spectra of Ru in Ru foil, $RuO_2$, $Ru_{(anc)}$-$Co_3O_4$ and $Ru_{(ads)}$-$Co_3O_4$. (c) The normalized XANES spectra and (b) first derivative spectra at Co K-edge of Co foil, $Co_3O_4$-$V_{Co}$, $Ru_{(anc)}$-$Co_3O_4$ and $Ru_{(ads)}$-$Co_3O_4$.

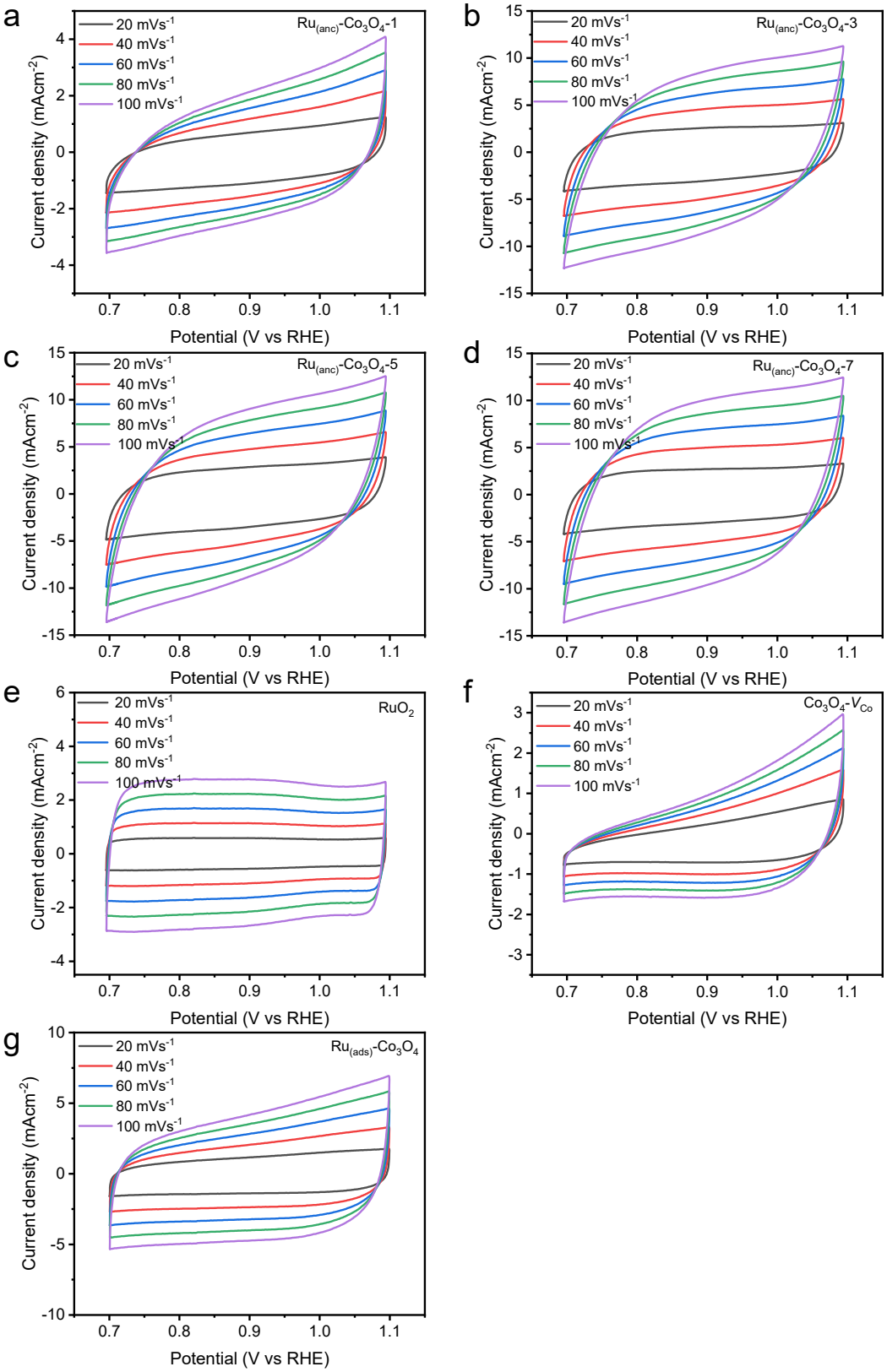


**Figure S15.** ECSA of various catalyst loadings on the electrode. (a-g) CV profiles of different catalyst loadings in the non-Faradaic region of 0.7 - 1.1 V vs. RHE with the scan rate of 20, 40, 60, 80, 100 mV $s^{-1}$.

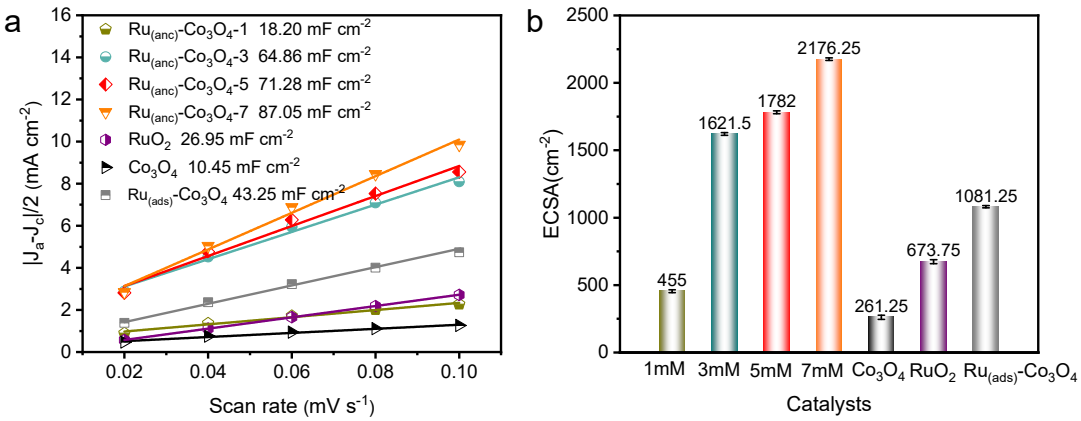


**Figure S16.** (a) $C_{dl}$ plots and (b) the detailed active surface area values obtained from the CV curves.

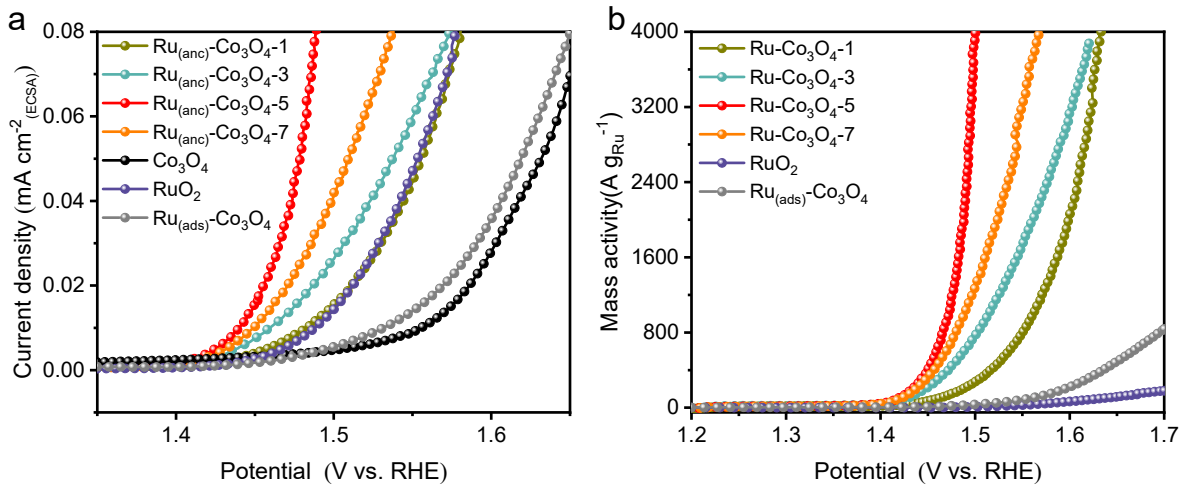


**Figure S17.** A comparison of (a) specific activity and (b) mass activity of $RuO_2$, $Co_3O_4$-$V_{Co}$, $Ru_{(anc)}$-$Co_3O_4$-X and $Ru_{(ads)}$-$Co_3O_4$.

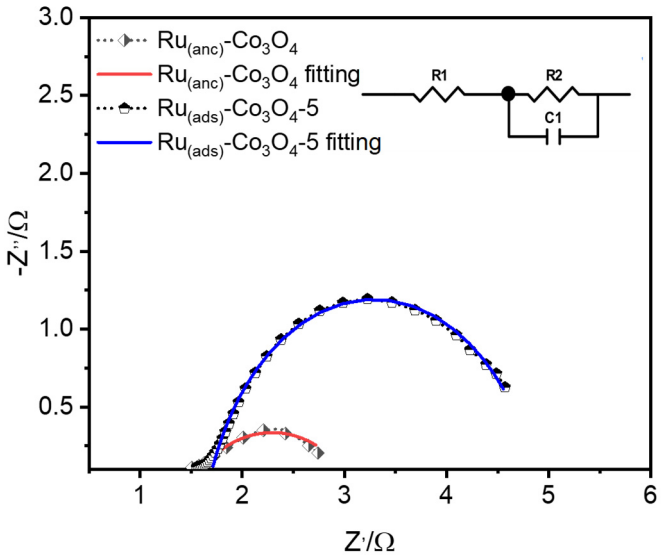


**Figure S18.** Nyquist plots of $Ru_{(anc)}$-$Co_3O_4$ and $Ru_{(ads)}$-$Co_3O_4$ for OER. The inset shows equivalent circuit models for OER.

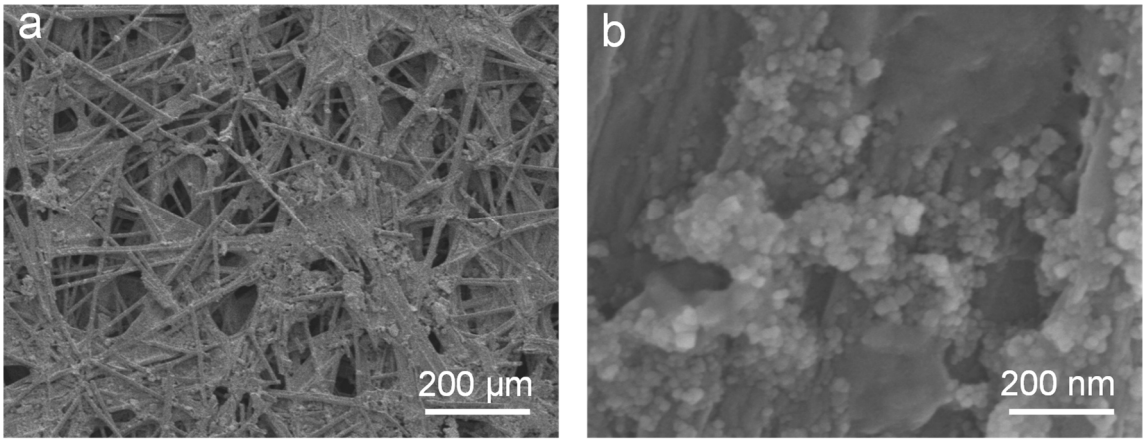


**Figure S19.** Evolution of $Ru_{(anc)}$-$Co_3O_4$ during acidic OER. (a-b) SEM image of $Ru_{(anc)}$-$Co_3O_4$ after the stability test at different magnifications.

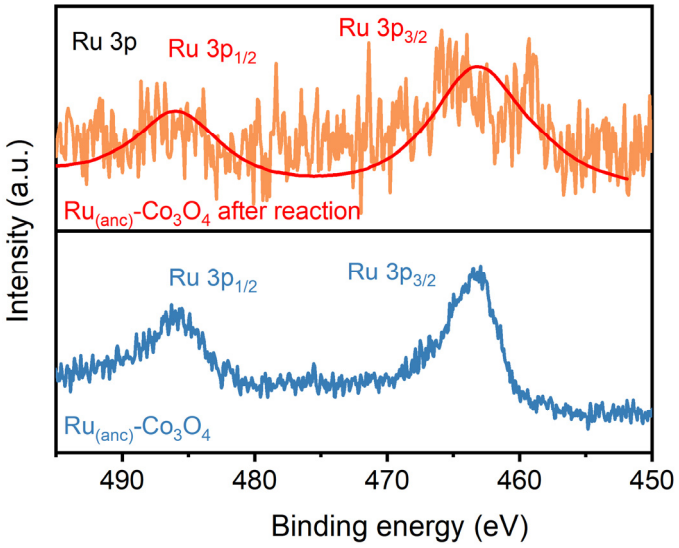


**Figure S20.** XPS spectra of Ru 3p regions for $Ru_{(anc)}$-$Co_3O_4$ before and after stability test.

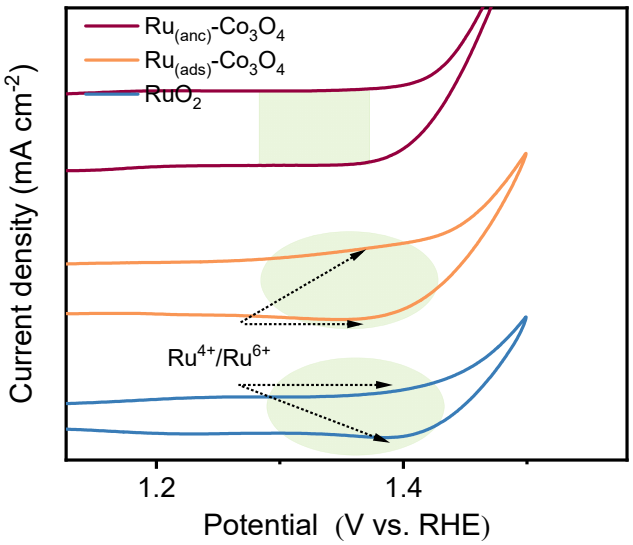


**Figure S21.** A comparison of the cyclic voltammograms curves without iR-corrected measured in argon-saturated 0.5 M $H_2SO_4$ at 50 mV s-1 for $RuO_2$, $Co_3O_4$-$V_{Co}$, $Ru_{(ads)}$-$Co_3O_4$ and $Ru_{(anc)}$-$Co_3O_4$.

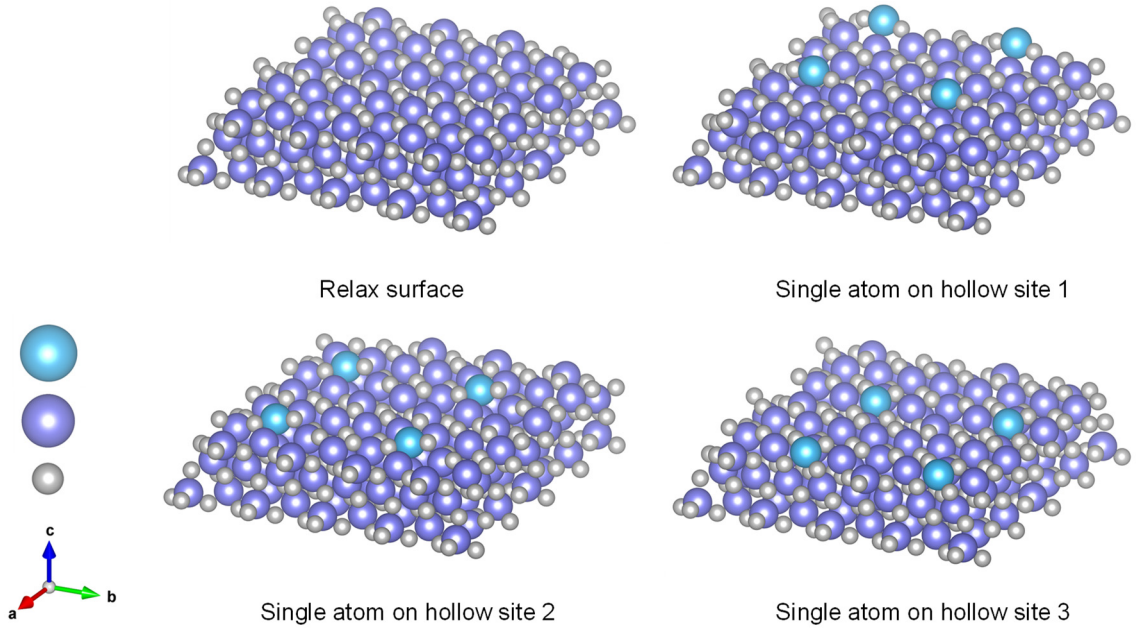


**Figure S22.** Single atoms anchored on different surface sites of $Co_3O_4$.

The adsorption energy of the ruthenium atoms was calculated at different positions on the surface and found that Ru was more likely to be stable in the interstices consisting of Co-O tetrahedra*2 and octahedra.

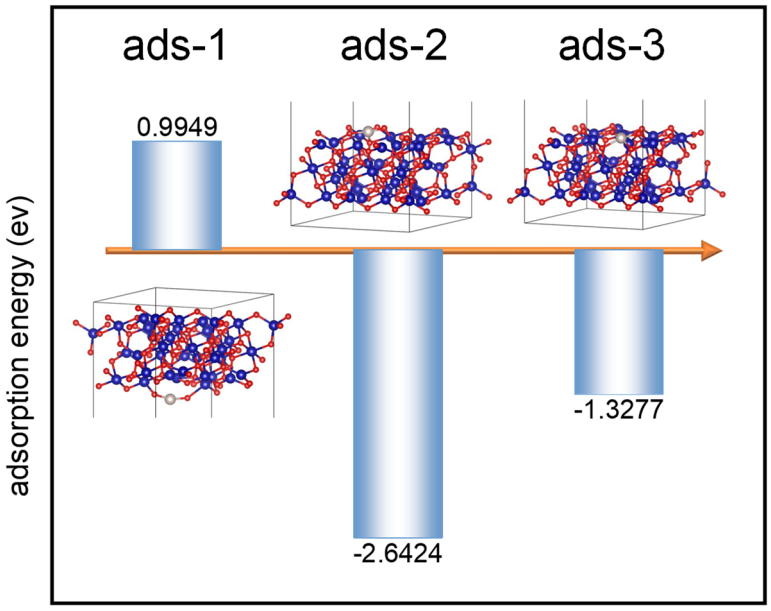


**Figure S23.** The Ru atom adsorption energy on different surface O sites. Ru was evaluated to adsorb more readily in the ads-2 model with two Co-O tetrahedra and an octahedron forming the gap.

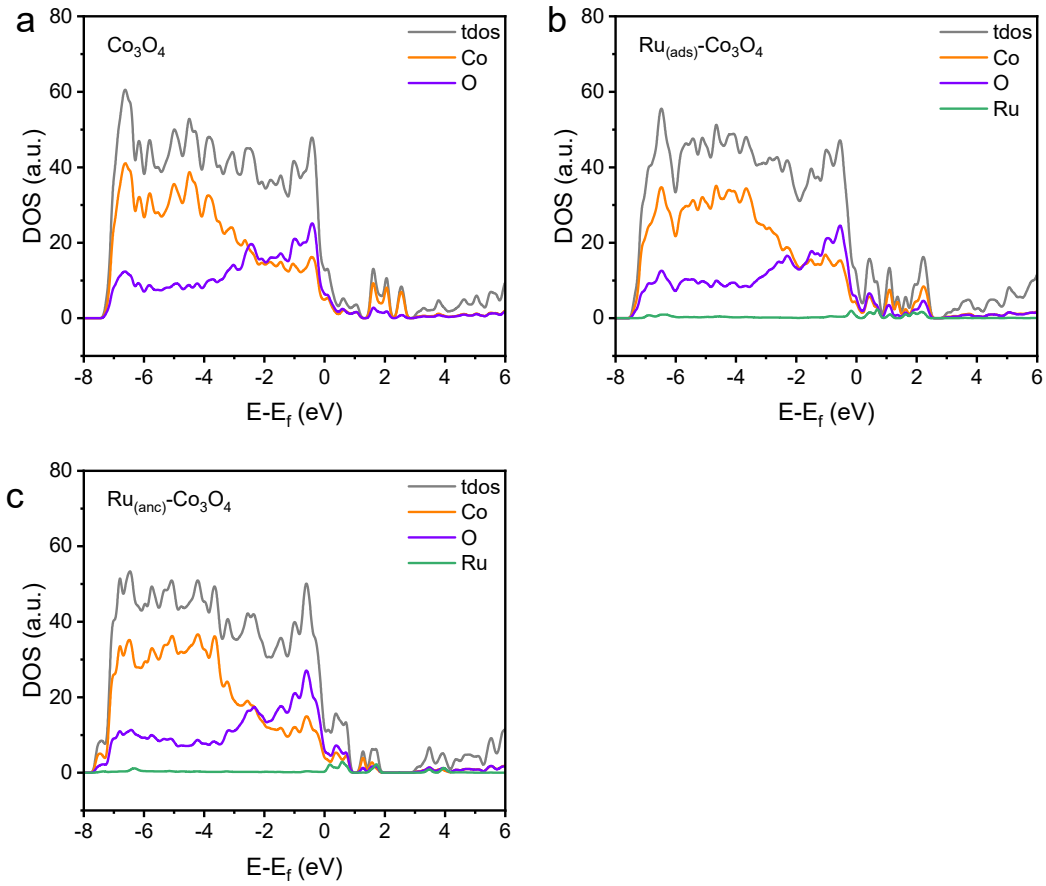


**Figure S24.** Corresponding Co, O and Ru PDOS and TDOS spectra of (a) $Co_3O_4$ (b) $Ru_{(ads)}$-$Co_3O_4$ and (c) $Ru_{(anc)}$-$Co_3O_4$.

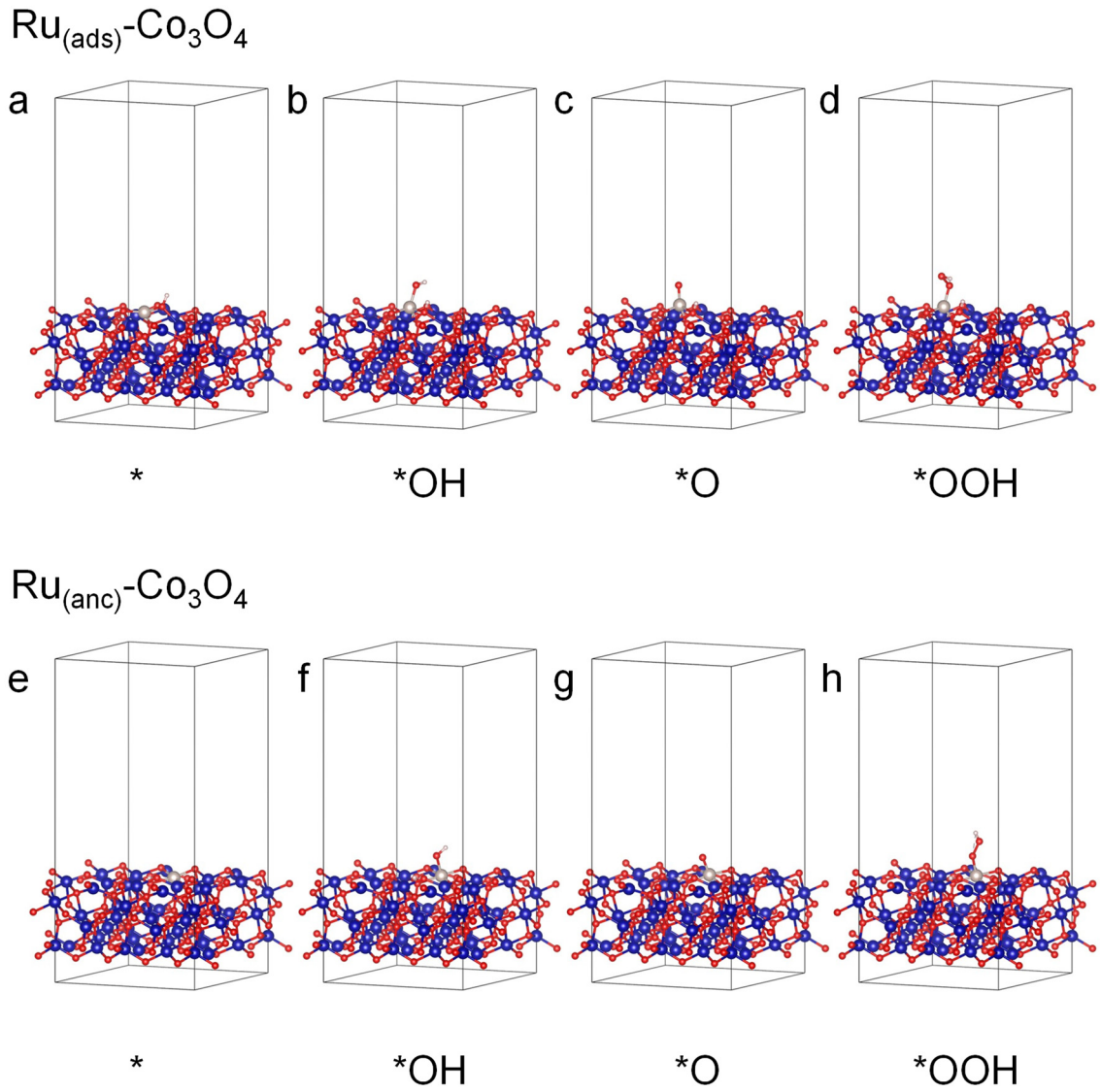


**Figure S25.** Local structural configurations of initial reactant, intermediates, and final product on the $Ru_{(ads)}$-$Co_3O_4$ (a-d) and $Ru_{(anc)}$-$Co_3O_4$ (e-h) in the AEM pathway.

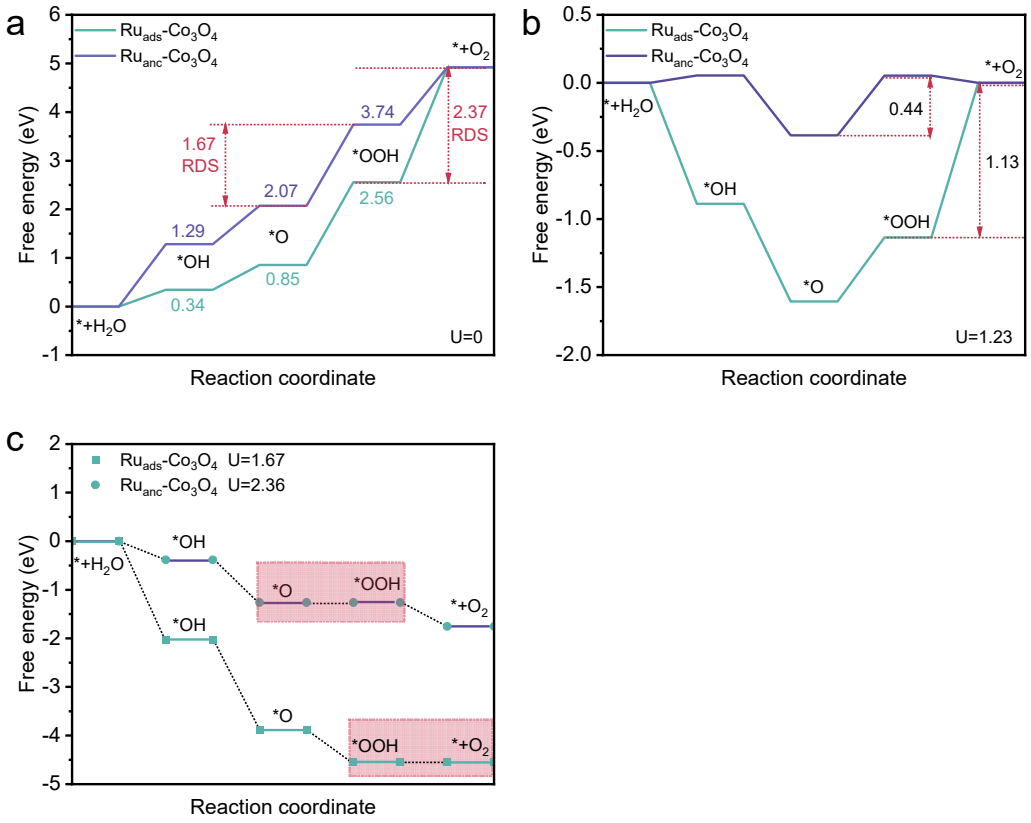


**Figure S26.** (a) The hypothetical AEM pathways of both four-electron-based acidic OER at U = 0 V. (b) The OER pathways are summarized at U = 1.23 V. (c) The OER pathways are summarized at 1.67 V and 2.36 V.

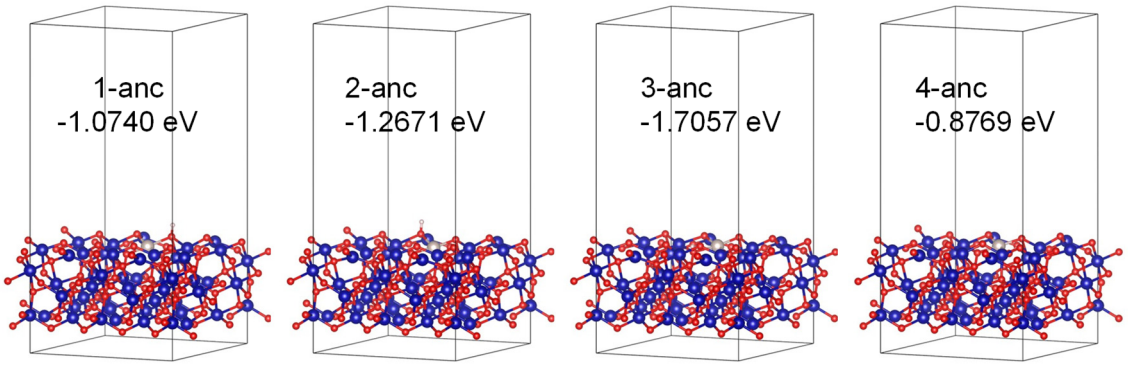


**Figure S27.** DFT investigation of hydrogen adsorption on Ru-anchored cobalt oxides. (a-d) Schematic of different Obri sites on the Ru-anchored $Co_3O_4$.

H is more likely to adsorb on the bridge oxygen for adsorption in the 3-anc model. The subsequent calculation of the AEM mechanism with the introduction of chemical steps was performed using the 3-anc model.

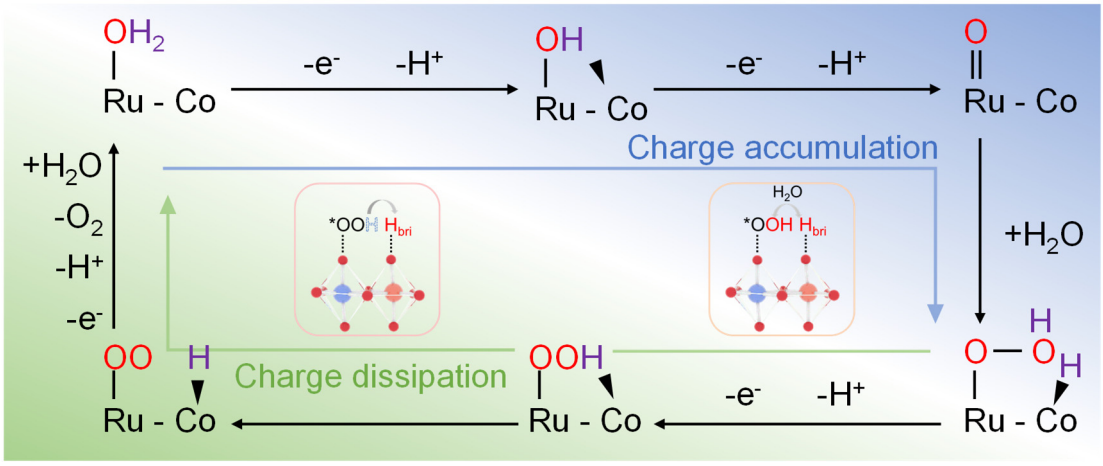


**Figure S28.** Proposed OER mechanism on the $Ru_{(anc)}$-$Co_3O_4$ under acidic conditions.

During the catalytic cycle, a concerted one proton ($H^+$) and one electron ($e^-$) transfer takes place as the quasi-equilibrium step. In the proposed mechanism, the Ru valence showed a reversible change with chemical bond rearrangement, indicating that the electrochemical OER could be a complementary process with charge accumulation and dissipation of the electrocatalyst.

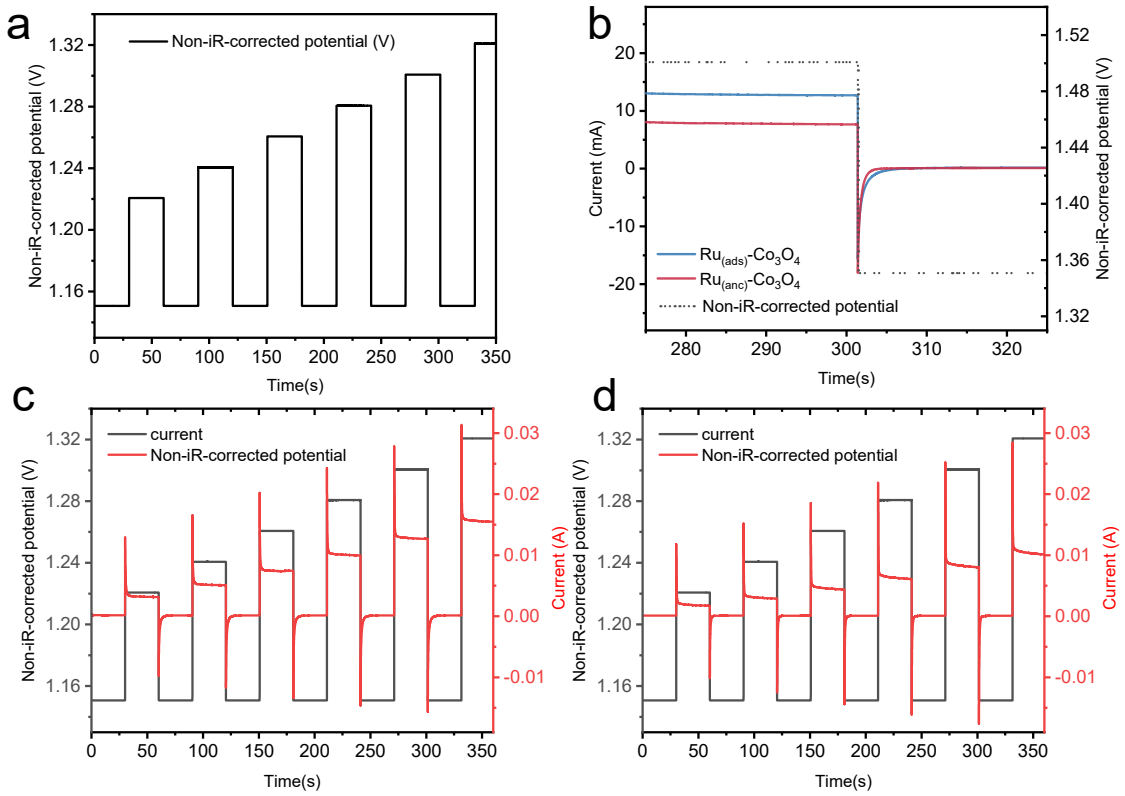


**Figure S29.** Pulse voltammetry protocol and response. (a) Pulse voltammetry protocol between 1.15 V cathodic and 1.22 V to 1.30 V (vs. Ag/AgCl) anodic non-iR corrected potentials. (b) Representative pulse voltammetry protocol showing the oxidative potential-OCP step and the corresponding pulse current response. Section of the pulse voltammetry protocol (black) showing an oxidative and reductive pulse with the current response (red) for (c) Ru(anc)-$Co_3O_4$ and (d) Ru(ads)-$Co_3O_4$.

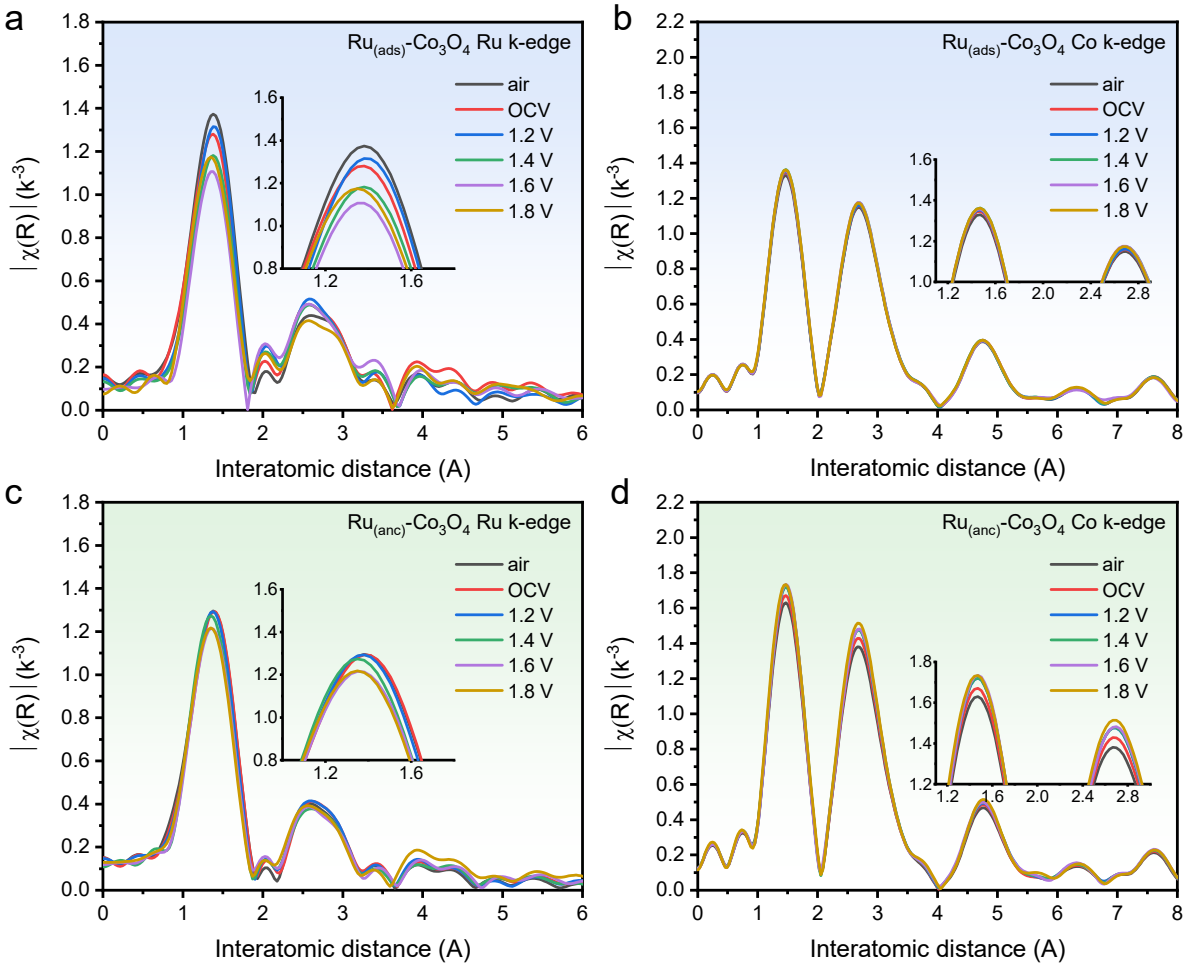


**Figure S30.** (a-b) In situ XANES spectra and In situ EXAFS spectra of $Ru_{(ads)}$-$Co_3O_4$. (c-d) In situ XANES spectra and In situ EXAFS spectra of $Ru_{(anc)}$-$Co_3O_4$.

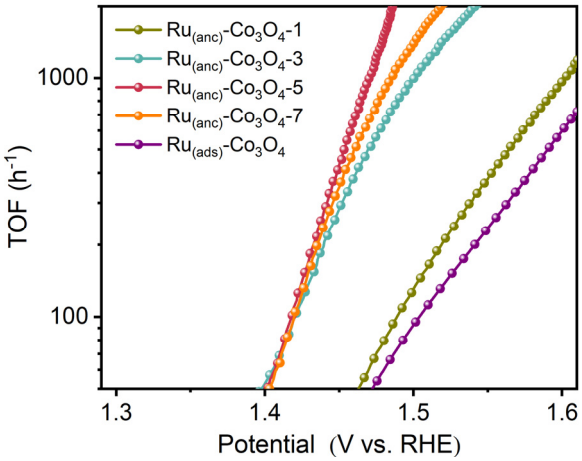


**Figure. S31.** The turnover frequency of the $Ru_{(ads)}$-$Co_3O_4$, $Ru_{(anc)}$-$Co_3O_4$-1, $Ru_{(anc)}$-$Co_3O_4$-3, $Ru_{(anc)}$-$Co_3O_4$-5 and $Ru_{(anc)}$-$Co_3O_4$-7 catalysts calculated from polarization curves.

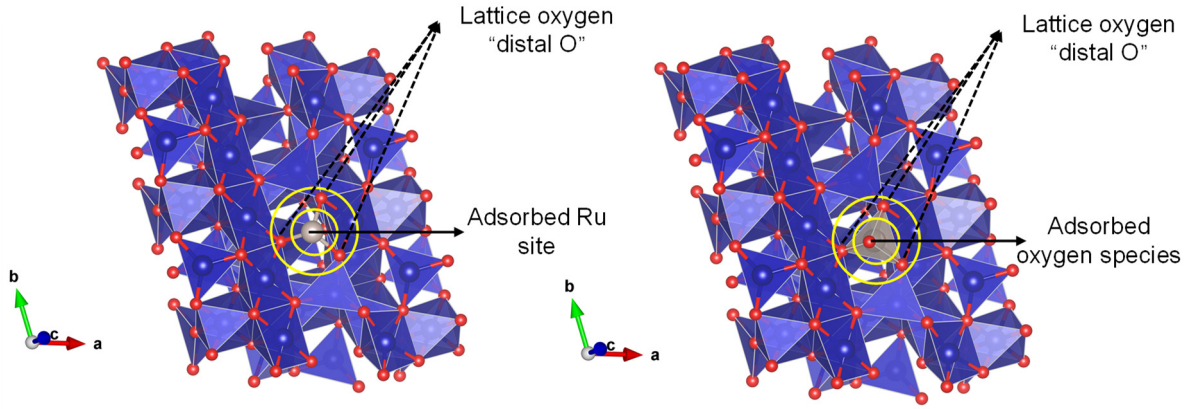


**Figure S32.** Structural modeling diagram of $Ru_{(ads)}$-$Co_3O_4$ distal and adsorbed oxygen in the LOM mechanism.

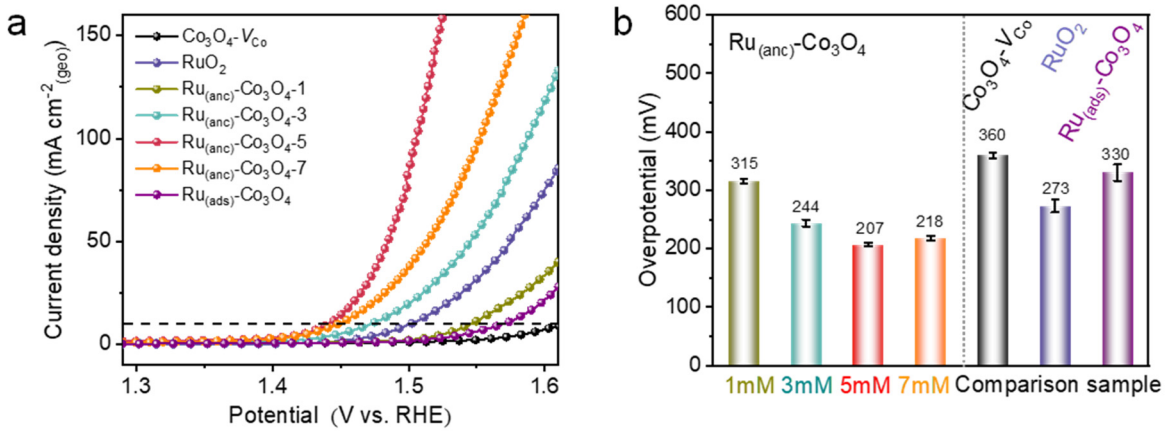


**Figure S33.** Oxygen evolution reaction activities in 0.5 M $H_2SO_4$ solution. (a) Oxygen evolution reaction polarization curves at a scan rate of 5 mV $s^{-1}$ for $RuO_2$, $Co_3O_4$-$V_{Co}$, $Ru_{(ads)}$-$Co_3O_4$, and $Ru_{(anc)}$-$Co_3O_4$-X. (without carbon black) (b) overpotential histogram and calculated from the iR-corrected polarization curves.

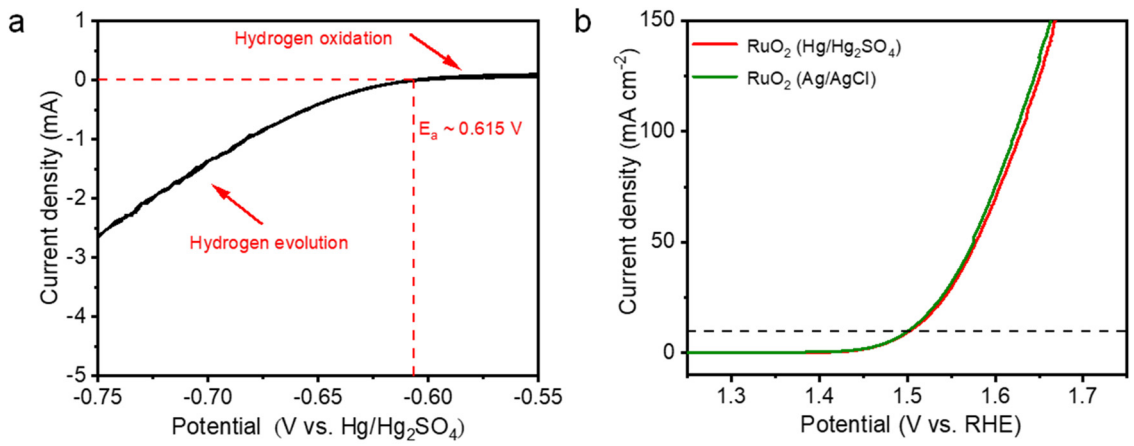


**Figure S34.** (a) RHE calibration plot. (b) Electrocatalytic OER performance of benchmark catalysts tested by Ag/AgCl electrodes and standard $Hg/Hg_2SO_4$ electrodes.

**Table S1.** The molar ratio of Ru and Co in the catalysts obtained by ICP.

| catalysts | Ru mass ratio among elements | Ru atomic ratio among metals | Co/Ru atomic ratio |
|---|---|---|---|
| $Ru_{(anc)}$-$Co_3O_4$-1 | 1.39% | 0.012 | 83.01:1 |
| $Ru_{(anc)}$-$Co_3O_4$-3 | 2.80% | 0.028 | 34.23:1 |
| $Ru_{(anc)}$-$Co_3O_4$-5 | 3.19% | 0.037 | 25.91:1 |
| $Ru_{(anc)}$-$Co_3O_4$-7 | 3.19% | 0.037 | 26.08:1 |
| $Ru_{(ads)}$-$Co_3O_4$ | 3.23% | 0.039 | 26.84:1 |

**Table S2.** A comparison of specific activity at 1.45 V, 1.47V and 1.49V versus RHE.

| | j at V=1.45 V ($mA\ cm^{-2}_{(ECSA)}$) | j at V=1.47 V ($mA\ cm^{-2}_{(ECSA)}$) | j at V=1.49 V ($mA\ cm^{-2}_{(ECSA)}$) |
|---|---|---|---|
| $Ru_{(anc)}$-$Co_3O_4$-1 | 0.0038 | 0.0074 | 0.0122 |
| $Ru_{(anc)}$-$Co_3O_4$-3 | 0.0074 | 0.0136 | 0.0214 |
| $Ru_{(anc)}$-$Co_3O_4$-5 | 0.0154 | 0.0359 | 0.0884 |
| $Ru_{(anc)}$-$Co_3O_4$-7 | 0.0099 | 0.0194 | 0.0327 |
| $Ru_{(ads)}$-$Co_3O_4$ | 0.0016 | 0.0025 | 0.0044 |
| $RuO_2$ | 0.0026 | 0.0054 | 0.0106 |
| $Co_3O_4$ | 0.0032 | 0.0036 | 0.0043 |

**Table S3.** A comparison of mass activity at 1.45 V, 1.47V and 1.49V versus RHE.

| | j at V=1.45 V ($A\ g^{-1}$) | j at V=1.47 V ($A\ g^{-1}$) | j at V=1.50 V ($A\ g^{-1}$) |
|---|---|---|---|
| $Ru_{(anc)}$-$Co_3O_4$-1 | 78.99 | 120.46 | 273.38 |
| $Ru_{(anc)}$-$Co_3O_4$-3 | 222.76 | 217.61 | 792.83 |
| $Ru_{(anc)}$-$Co_3O_4$-5 | 468.68 | 1112.23 | 4012.11 |
| $Ru_{(anc)}$-$Co_3O_4$-7 | 346.53 | 613.31 | 1344.92 |
| $Ru_{(ads)}$-$Co_3O_4$ | 0.66 | 5.25 | 36.96 |
| $RuO_2$ | 0.98 | 4.46 | 32.99 |

**Table S4.** Correlation of the equivalent resistances (R1 and R2) for $Ru_{(anc)}$-$Co_3O_4$ and $Ru_{(ads)}$-$Co_3O_4$ during OER.

| | R1 | R2 |
|---|---|---|
| $Ru_{(anc)}$-$Co_3O_4$ | 1.673 | 3.227 |
| $Ru_{(ads)}$-$Co_3O_4$-5 | 1.567 | 1.649 |

**Table S5.** Comparison of the OER single-atom electrocatalysts performance in acidic media.

| Electrocatalyst | Overpotential @10 mA $cm^{-2}$ (mV) | Electrolyte | Ref. |
|---|---|---|---|
| **$Ru_{(anc)}$-$Co_3O_4$** | **198** | **0.5 M $H_2SO_4$** | **This work** |
| **$Ru_{(ads)}$-$Co_3O_4$** | **298** | **0.5 M $H_2SO_4$** | **This work** |
| Ru-$Pt_3Cu$ | 220 | 0.1 M $HClO_4$ | Nat. Catal. 2019, 2, 304-313 |
| $Ir_{0.06}Co_{2.94}O_4$ | 294 | 0.1 M $HClO_4$ | J. Am. Chem. Soc. 2021, 143, 5201-5211 |
| Ir-$NiCo_2O_4$ NSs | 240 | 0.5 M $H_2SO_4$ | J. Am. Chem. Soc. 2020, 142, 18378-18386 |
| Ru-N-C | 267 | 0.5 M $H_2SO_4$ | Nat. Commun. 2019, 10, 4849 |
| AD-HN-Ir | 216 | 0.5 M $H_2SO_4$ | Nat. Commun. 2021, 12, 6118 |
| Ir-$Co_3O_4$ | 236 | 0.5 M $H_2SO_4$ | Nat. Commun. 2022, 13, 7754 |
| Ru/Co-N-C | 232 | 0.5 M $H_2SO_4$ | Adv. Mater. 2022, 34, 2110103 |
| Ir-$MnO_2$ | 218 | 0.5 M $H_2SO_4$ | Joule 2021, 5, 2164-2176 |
| Ir-SA@Fe@NCNT | 250 | 0.5 M $H_2SO_4$ | Nano Lett. 2020, 20, 2120-2128 |
| Pd-$Pt_3Sn$ | 270 | 0.5 M $H_2SO_4$ | Chem. Commun. 2021, 57, 11561-11564 |
| Ru-SA/$Ti_3C_2T_x$ | 290 | 0.1 M $HClO_4$ | Small 2020, 16, 2002888 |
| HNC-Co | 265 | 0.5 M $H_2SO_4$ | ACS Energy Lett. 2019, 4, 1816-1822 |
| Pt1-$C_2N_2$ SAC | 232 | 0.5 M $H_2SO_4$ | eScience 2022, 2, 102-109 |
| Ir-$Co_3O_4$-NS-350 | 226 | 0.5 M $H_2SO_4$ | ACS Catal. 2023, 13, 3757-3767 |
| $CoCl_2$@Th-BPYDC | 388 | 0.1 M $HClO_4$ | ACS Catal. 2022, 12, 9101-9113 |

Table S6. The turnover frequency of the $Ru_{(ads)}$-$Co_3O_4$, $Ru_{(anc)}$-$Co_3O_4$-1, $Ru_{(anc)}$-$Co_3O_4$-3, $Ru_{(anc)}$-$Co_3O_4$-5 and $Ru_{(anc)}$-$Co_3O_4$-7 catalysts at 1.48 V.

| catalysts | TOF @ 1.48 V | TOF @ 1.50 V |
|---|---|---|
| $Ru_{(ads)}$-$Co_3O_4$ | 60.34 | 94.43 |
| $Ru_{(anc)}$-$Co_3O_4$-1 | 79.56 | 126.88 |
| $Ru_{(anc)}$-$Co_3O_4$-3 | 636.28 | 978.34 |
| $Ru_{(anc)}$-$Co_3O_4$-5 | 1570.70 | 4046.60 |
| $Ru_{(anc)}$-$Co_3O_4$-7 | 870.11 | 1403.42 |